Direct Observational Evidence of the Multi-scale, Dynamical Mass Accretion Toward a High-mass Star-forming Hub-filament System

Dongting Yang, Hong-Li Liu, Anandmayee Tej, Tie Liu, Patricio Sanhueza, Sheng-Li Qin, Xing Lu, Ke Wang, Sirong Pan, Feng-Wei Xu, et al.

The Astrophysical Journal, 953:40 (9pp), 2023 August 10 https://doi.org/10.3847/1538-4357/acdf42

Direct Observational Evidence of the Multi-scale, Dynamical Mass Accretion Toward a High-mass Star-forming Hub-filament System

Dongting Yang[1], Hong-Li Liu[1], Anandmayee Tej[2], Tie Liu[3,4], Patricio Sanhueza[5,6], Sheng-Li Qin[1], Xing Lu[3], Ke Wang[7,8], Sirong Pan[1], Feng-Wei Xu[7,8], Enrique Vázquez-Semadeni[9], Shanghuo Li[10], Gilberto C. Gómez[9], Aina Palau[9], Guido Garay[11], Paul F. Goldsmith[12], Mika Juvela[13], Anindya Saha[2], Leonardo Bronfman[11], Chang Won Lee[14,15], Ken'ichi Tatematsu[5,6], Lokesh Dewangan[16], Jianwen Zhou[10], Yong Zhang[17], Amelia Stutz[10,18], Chakali Eswaraiah[19], L. Viktor Toth[20], Isabelle Ristorcelli[21], Xianjin Shen[1], Anxu Luo[1], and James O. Chibueze[22,23,24]
[1] School of Physics and Astronomy, Yunnan University, Kunming, 650091, People's Republic of China; hongliliu2012@gmail.com
[2] Indian Institute of Space Science and Technology, Thiruvananthapuram 695 547, Kerala, India; tej@iist.ac.in
[3] Shanghai Astronomical Observatory, Chinese Academy of Sciences, 80 Nandan Road, Shanghai 200030, People's Republic of China
[4] Key Laboratory for Research in Galaxies and Cosmology, Shanghai Astronomical Observatory, Chinese Academy of Sciences, 80 Nandan Road, Shanghai 200030, People's Republic of China
[5] National Astronomical Observatory of Japan, National Institutes of Natural Sciences, 2-21-1 Osawa, Mitaka, Tokyo 181-8588, Japan
[6] Astronomical Science Program, Graduate Institute for Advanced Studies, SOKENDAI, 2-21-1 Osawa, Mitaka, Tokyo 181-8588, Japan
[7] Kavli Institute for Astronomy and Astrophysics, Peking University, 5 Yiheyuan Road, Haidian District, Beijing 100871, People's Republic of China
[8] Department of Astronomy, Peking University, 100871, Beijing, People's Republic of China
[9] Instituto de Radioastronomía y Astrofísica, Universidad Nacional Autónoma de México, Antigua Carretera a Pátzcuaro 8701, ExHda. San José de la Huerta, Morelia, Michoacán, C.P. 58089, México
[10] Max Planck Institute for Astronomy, Königstuhl 17, D-69117 Heidelberg, Germany
[11] Departamento de Astronomía, Universidad de Chile, Casilla 36-D, Santiago, Chile
[12] Jet Propulsion Laboratory, California Institute of Technology, 4800 Oak Grove Drive, Pasadena, CA 91109, USA
[13] Department of Physics, PO box 64, FI-00014, University of Helsinki, Helsinki, Finland
[14] Korea Astronomy and Space Science Institute, 776 Daedeokdaero, Yuseonggu, Daejeon 34055, Republic of Korea
[15] University of Science and Technology, Korea (UST), 217 Gajeong-ro, Yuseong-gu, Daejeon 34113, Republic of Korea
[16] Physical Research Laboratory, Navrangpura, Ahmedabad 380 009, India
[17] School of Physics and Astronomy, Sun Yat-sen University, 2 Daxue Road, Zhuhai, Guangdong, 519082, People's Republic of China
[18] Departamento de Astronomía, Universidad de Concepción, Av. Esteban Iturra s/n, Distrito Universitario, 160-C, Chile
[19] Indian Institute of Science Education and Research Tirupati, Rami Reddy Nagar, Karakambadi Road, Mangalam (P.O.), Tirupati 517 507, India
[20] Eötvös Loránd University, Department of Astronomy, Pázmány Péter sétány 1/A, H-1117, Budapest, Hungary
[21] IRAP, Université de Toulouse, CNRS, UPS, CNES, Toulouse, France
[22] Centre for Space Research, North-West University, Potchefstroom 2520, South Africa
[23] Department of Mathematical Sciences, University of South Africa, Cnr Christian de Wet Rd and Pioneer Avenue, Florida Park, 1709, Roodepoort, South Africa
[24] Department of Physics and Astronomy, Faculty of Physical Sciences, University of Nigeria, Carver Building, 1 University Road, Nsukka 410001, Nigeria; tej@iist.ac.in

Received 2023 March 4; revised 2023 May 24; accepted 2023 June 16; published 2023 August 1

Abstract

There is growing evidence that high-mass star formation and hub-filament systems (HFS) are intricately linked. The gas kinematics along the filaments and the forming high-mass star(s) in the central hub are in excellent agreement with the new generation of global hierarchical high-mass star formation models. In this paper, we present an observational investigation of a typical HFS cloud, G310.142+0.758 (G310 hereafter), which reveals unambiguous evidence of mass inflow from the cloud scale via the filaments onto the forming protostar(s) at the hub conforming with the model predictions. Continuum and molecular line data from the ATOMS and MALT90 surveys that cover different spatial scales are used. Three filaments (with a total mass of $5.7 \pm 1.1 \times 10^3\ M_\odot$) are identified converging toward the central hub region where several signposts of high-mass star formation have been observed. The hub region contains a massive clump ($1280 \pm 260\ M_\odot$) harboring a central massive core. Additionally, five outflow lobes are associated with the central massive core implying a forming cluster. The observed large-scale, smooth, and coherent velocity gradients from the cloud down to the core scale, and the signatures of infall motion seen in the central massive clump and core, clearly unveil a nearly continuous, multi-scale mass accretion/transfer process at a similar mass infall rate of $\sim 10^{-3}\ M_\odot\ \mathrm{yr}^{-1}$ over all scales, feeding the central forming high-mass protostar(s) in the G310 HFS cloud.

Unified Astronomy Thesaurus concepts: Star forming regions (1565); Molecular clouds (1072); Infrared dark clouds (787); Young stellar objects (1834); Molecular gas (1073); Dust continuum emission (412)

1. Introduction

Filamentary molecular clouds are not only observed to be ubiquitous in the interstellar medium (ISM), but are intimately related to star formation (André et al. 2010; Molinari et al. 2010). Of crucial importance is the special web of filaments known as the hub-filament systems (HFSs), which have opened a whole new window to probe the initial stages of high-mass star formation (Myers 2009; Kumar et al. 2020; Liu et al. 2023). The HFS comprises at least three filaments apparently converging toward the central web node, which is defined as the hub while the associated individual filaments as the hub-composing filaments

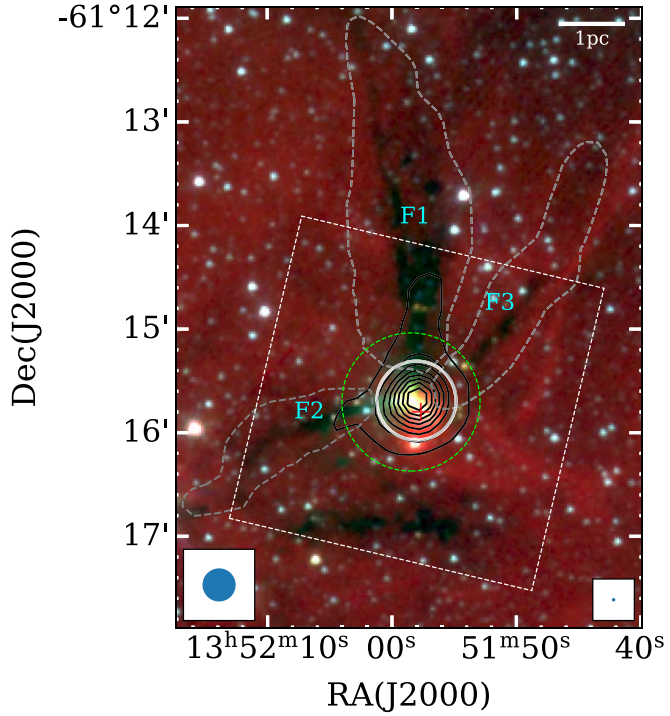

Figure 1. Three-color composite image of Spitzer 8.0 μm (red), 4.5 μm (green), and 3.6 μm (blue) overlaid with ATLASGAL 870 μm continuum emission (in contours). The three filaments seen as dark dust lanes against bright background emission are labeled F1–F3. The contour levels start at 3 rms with the steps given by the power law $D = 3 \times N^p + 2$, where the dynamical range (D) of the intensity map is defined as the ratio of the peak intensity to the rms, N is the number of the contour levels ($N = [1, 8]$ in this case), and the index p is derived from the maximum N and D. The red cross shows the location of the UC-H II region (Purser et al. 2018). The white circle shows the extent of the central massive 870 μm clump. The white box and the green circle represent the field view of the MALT90 and ATOMS data, respectively. The polygons (gray dashed line) roughly outline the filamentary structures (F1–F3) based on the $N(H_2)$ column density map. The beam sizes of 8.0 and 870 μm are displayed at the bottom right and bottom left corners, respectively.

(Myers 2009; Kumar et al. 2020; Liu et al. 2023). From the theoretical perspective, the latest generation of star formation models, such as *global hierarchical collapse* (GHC; Vázquez-Semadeni et al. 2019) and *inertial inflow* (I2; Padoan et al. 2020), advocate the multi-scale mass accretion scenario from clouds to the seeds of star formation. Here, HFSs work as *conveyor belts* to transport gas material from large-scale clouds, through hub-composing filaments, to central hubs and further to smaller scales (i.e., cores, and seeds of star formation). Although this scenario has been strongly supported by recent multi-scale observational and statistical studies (Kumar et al. 2020; Zhou et al. 2022; Liu et al. 2023), GHC advocates a cloud-scale gravitational origin of the flows assembling the HFS, while I2 advocates a turbulent origin. For this reason, the kinetic energy is expected to dominate at the clump scale in the I2 model, while gravitational energy should dominate up to the cloud scale according to GHC.

This study is focused on the HFS cloud G310.142+0.758 (hereafter G310). It is selected from Liu et al. (2023) owing to its distinct HFS structure visible in Spitzer 8.0 μm emission (see Figure 1), where a network of three filaments (F1–F3) appear as dark lanes converging toward the cloud center (defined as the peak of 870 μm emission as shown in contours in the figure). A dark east–west filament is visible to the south and does not reveal any apparent connecting feature to the central hub. Hence, we do not consider this filament in our analysis of the HFS. In addition, the F1 filament seems to contain subfilaments, but are treated here as one entity (see Section 3.5). Several distance estimates are available in the literature for G310. Liu et al. (2021) estimated the distance to be $6.9^{+0.5}_{-0.7}$ kpc. These authors used the Reid et al. (2014) rotation curve with the updated solar motion parameters (Reid et al. 2019) and the Monte Carlo technique with 10,000 samplings (Wenger et al. 2018). In this paper, we adopt the distance estimate of 5.4 ± 0.5 kpc used by many authors (Bronfman et al. 1996; Purser et al. 2018; Liu et al. 2020a). This estimate is based on the Brand & Blitz (1993) Galactic rotation curve. Following Urquhart et al. (2014) and Sanhueza et al. (2017), we allow for ∼10% uncertainty. G310 manifests ongoing high-mass star formation, as characterized by its associated, centrally located luminous IRAS source I13484-6100 with $L_{bol} \sim 10^{4.8}\ L_\odot$ (Bronfman et al. 1996). The presence of a cometary ultracompact (UC) H II region (G310.1420 +00.7583B, Purser et al. 2018), detection of maser emission from different species such as OH, H_2O, and CH_3OH (6.7 GHz, Class II) masers (Walsh et al. 1998; Urquhart et al. 2009; Green et al. 2012), an extended green object (EGO; Cyganowski et al. 2008), and radio jets (Purser et al. 2018) makes the G310 HFS cloud an ideal target for addressing the mechanisms involved in high-mass star formation by studying the hierarchical kinematics and dynamics covering different scales from clouds to cores.

2. Observations

The hub of the G310 HFS cloud (see Figure 1) was observed as part of the ATOMS (ALMA Three-millimeter Observations of Massive Star-forming regions; Liu et al. 2020a, 2020b, 2021) survey. Combined 7+12 m continuum and line emission data at 3 mm are used here, which offers a field of view of ∼80″ or 2.1 pc at the distance of G310, and a maximum recoverable scale of ∼60″ or 1.6 pc. We utilize HCO^+ and $H^{13}CO^+$ (1–0) spectral line data to probe the kinematics and dynamics of dense gas and the SiO (2–1) and CS (2–1) transitions to trace the shocked gas. The synthesized beam size is $2\farcs7 \times 2\farcs0$ for the continuum and $H^{13}CO^+$spectral line and $3\farcs1 \times 2\farcs3$ for the other spectral lines investigated here. These values correspond to 0.06 and 0.07 pc at the distance of G310. In addition, the data sensitivity is ∼0.3 mJy beam^{-1} for the continuum, and ∼ [12, 8, 3] mJy beam^{-1} for the [HCO^+, $H^{13}CO$/SiO, CS] lines at a native velocity resolution of [0.1, 0.2, 1.5] km s^{-1}.

Additionally, Spitzer 3.6, 4.5, and 8.0 μm images retrieved from the GLIMPSE survey (Benjamin et al. 2003) are used to facilitate the identification of the HFS morphology of G310 (Figure 1). These images have angular resolutions better than 2″ (Benjamin et al. 2003) that nearly match the resolution of the ATOMS data used here. Further, to explore the dynamics (i.e., velocity gradients and infall motions) of the cloud and clump scales, we use the 3′ × 3′–sized maps of HCO^+ and $H^{13}CO^+$ (1–0) obtained from the Millimeter Astronomy Legacy Team 90 GHz (MALT90) survey (Foster et al. 2011, 2013; Jackson et al. 2013). These data have an angular resolution of 38″ or 1.0 pc, and a sensitivity of 0.25 K at a spectral resolution of 0.11 km s^{-1} (Jackson et al. 2013).

3. Results and Analysis

3.1. Continuum Emission

The HFS morphology seen in the mid-infrared is also revealed in the submillimeter and millimeter dust emission

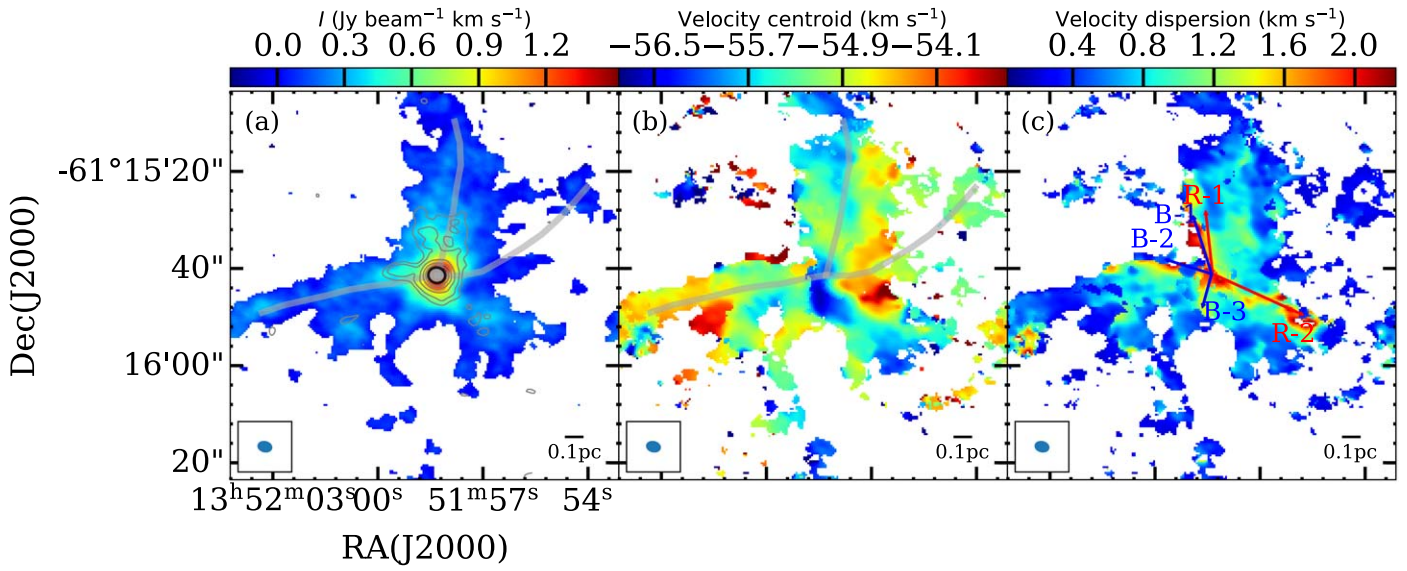

Figure 2. Moment maps of $H^{13}CO^+$ (1–0) from the ATOMS data for the central hub region of G310. (a) Integrated intensity (moment 0) map overlaid with the ATOMS 3 mm continuum contours. The contour levels follow the same trend as that in Figure 1. The central massive core is indicated by a gray ellipse with a black edge. (b) Mean velocity (moment 1) map. The gray thick line shows the filaments of the G310 HFS cloud in panels (a) and (b). (c) Velocity dispersion (moment 2) map. The blue and red arrows show the blue- and redshifted outflow lobes (i.e., R-1/2 and B-1/2/3), respectively. The ALMA beam size is shown in the bottom left.

Table 1
Physical Properties of the Central Clump and the Central Core in HFS G310

Name	R. A.	Decl.	Radius (pc)	T_{dust} K	Mass ($M_\odot$)	α_{vir}	V_{infall} (km s^{-1})	$\dot{M}_{infall}$ ($10^{-3} \times M_\odot$ yr^{-1})	Data Source
Central clump	13:51:57.76	−61:15:43.72	0.6	31.8	1280 ± 260	0.4 ± 0.1	1.1 ± 0.6	2.4 ± 1.7	Mopra
Central core	13:51:58.30	−61:15:41.40	0.036	100	106 ± 21	1.5 ± 0.6	2.1 ± 0.1	6.5 ± 1.3	ATOMS

Notes. Column 1: source name; Column 2: radius of clump or core; Column 3: dust temperature (see text in Section 3.1); Column 4: mass; Column 5: viral parameter; Column 6: infall velocity; Column 7: mass accretion rate.

maps. The 870 μm dust emission obtained from the ATLASGAL survey (Schuller et al. 2009) is shown in Figure 1, where the signature of filaments F1 and F2 extend outward and the centrally located, massive clump is clearly discernible. The higher resolution ATOMS 3 mm dust emission contours also trace the inner part of these filaments, which originate from the central massive core (see Figure 2(a)).

We estimate the mass of the ATLASGAL clump following Equation B1 of Liu et al. (2021). We define a circular region of radius 0.6 pc (white circle in Figure 1) that encloses most of the 870 μm emission (∼8.7 Jy). Assuming a dust opacity of 0.0178 cm^2 g^{-1} that accounts for a gas-to-dust gas mass ratio of 100 (Ossenkopf & Henning 1994), clump mass is estimated to be $1280 \pm 260\,M_\odot$ for a given clump-average temperature of 31.8 K (Bronfman et al. 1996; Faúndez et al. 2004), where the error comes mostly from the uncertainty in the distance estimate. The mass of the candidate hot molecular core (HMC; Liu et al. 2021), i.e., central massive core (radius of 0.036 pc), mass is estimated to be $106 \pm 21\,M_\odot$ at an assumed temperature of 100 K. Given the non-detection of H40α line emission from the central massive core (Liu et al. 2021), the 3 mm continuum can be considered to be mostly from thermal dust emission with negligible contamination from ionized gas (free–free emission). The estimated parameters for the central massive clump and the central core are listed in Columns 4–6 of Table 1.

3.2. $H^{13}CO^+$ (1–0) Line Emission

$H^{13}CO^+$ line emission is generally considered optically thin (Liu et al. 2022a, 2022b), and hence, a good tracer of kinematics/dynamics and density structures of different scales. In the analysis presented, the field of view of ATOMS is considered the central hub of the G310 HFS. The average spectrum of $H^{13}CO^+$ (1–0) over the central hub region is single peaked from which the systemic velocity is estimated to be $V_{lsr} = -55.2$ km s^{-1}. $H^{13}CO^+$ (1–0) moment maps, generated from a de-noised/modeled $H^{13}CO^+$ data cube (see Appendix A), are shown in Figure 2. As seen in the moment 0 map, the spatial distribution of $H^{13}CO^+$ (1–0) is much more extended compared to the 3 mm dust emission which is confined to the innermost region. Two of the overlaid (in gray) filament skeletons (F1 and F2) traced from the 8.0 μm image are discernible in the $H^{13}CO^+$ (1–0) emission (above 5 rms). An elongated gas emission is seen from the central core in the southwest direction. This is also visible as an IR-bright filament-like structure in the 8.0 μm emission (see Figure 1). As can be seen in Figure 2(c) and discussed later, this feature is cospatial with the outflow R-2 and hence likely associated with shocks from the outflow (De Buizer et al. 2017).

The velocity field, displayed in the moment 1 map, shows gradients along the filaments (i.e., F1–F3). In a later section (see Section 3.4), a detailed analysis of the filament velocity structure will be presented. Interestingly, a very local, radially

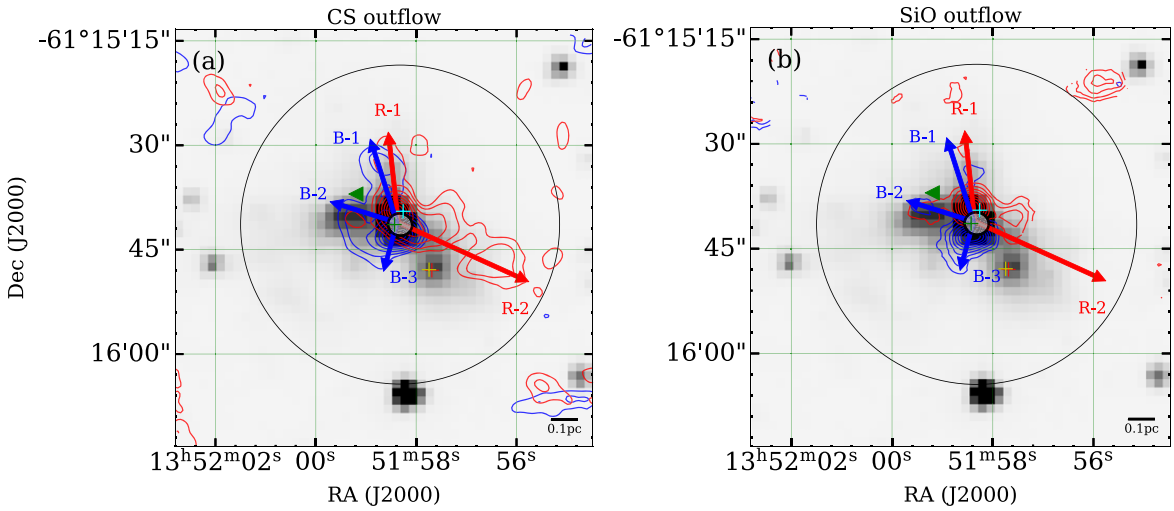

Figure 3. Panel (a) CS (2–1) outflows overlaid on the Spitzer 4.5 μm map. The contour levels start at 3 rms ($\sim$0.15 Jy beam^{-1} km s^{-1}), increased by steps following the same power law as in Figure 1. Panel (b) SiO (2–1) outflows overlaid on the Spitzer 4.5 μm map, the contour is the same as that in panel (a), but starts at 3 rms ($\sim$0.08 Jy beam^{-1} km s^{-1}). In both panels, the blue and red arrows show the blue- and redshifted outflowing lobes (i.e., R-1/2 and B-1/2/3), respectively. The 3 mm central massive core is shown as a gray ellipse. The black circle represents the central massive clump of radius 0.6 pc. The green triangle denotes the location of the identified EGO. The red cross shows the location of the UC-H II region, and the green, cyan, and yellow crosses represent the CH_3OH, OH, and H_2O masers, respectively.

symmetric velocity gradient can be found across the IR-bright filament discussed above.

The observed pattern of the velocity gradient can originate from various physical processes like disk rotation, the collision of local gas flows, and/or stellar feedback such as outflows and winds. The possibility of disk rotation can be ruled out since no Keplerian-like signature is found in the position–velocity (PV) diagram particularly made along the velocity gradient orientation (not presented in the paper). Although the possibility of the collision between gas flows cannot be completely rejected, a more plausible explanation is the outflow feedback since the red/blueshifted outflow lobes (see Figure 3, and Section 3.3) are found to be spatially coincident with the red/blueshifted velocity components of the local velocity gradient.

The moment 2 map (see Figure 2(c)) shows the velocity dispersion to be nonuniform with higher values in the inner region, implying active star-forming activity (e.g., outflows). Regions with high-velocity dispersion appear as a slingshot-like pattern cospatial with the identified outflow lobes (see Figure 2(c)). Quantitatively, the velocity dispersion of the entire hub region has a median value of 0.58 km s^{-1} ranging from 0.22–2.20 km s^{-1}. Following Liu et al. (2019), the typical value of the total turbulent velocity (including thermal and nonthermal contribution) is estimated to be 0.66 km s^{-1} taking the thermal speed as 0.34 km s^{-1} for a given clump-averaged temperature of 31.8 K. This result suggests that the central hub region of the G310 HFS cloud is overall supersonic.

3.3. Molecular Outflows

Two shocked gas tracers, CS (2–1) and SiO (2–1), are used for reliable identification of outflow lobes in the G310 HFS. From the line wings of the average spectrum of each transition over the central hub with significant emission (above 5 rms), the blue/redshifted outflowing gas is integrated over [−75, −60]/[−50, −35] km s^{-1} for CS (2–1), and [−85, −60]/[−50, −25] km s^{-1} for SiO (2–1).

Five outflow lobes are identified and presented in Figure 3(a) for the CS tracer and Figure 3(b) for SiO. These lobes show similar structures in both tracers though the spatial extent of CS emission is comparatively larger. It is possible that faint, extended SiO emission is below the sensitivity of the observations (about 0.2 K).

The identified outflows in both tracers are consistent with the detection of radio jets reported in Figure 4 in Purser et al. (2018), and the location of the associated EGO (Cyganowski et al. 2008, see Figure 3(a)). Of particular interest is the spatial extension of the outflowing lobe, R-2, oriented along the IR-bright filament discussed earlier.

Moreover, all outflowing lobes appear to originate from the most massive central core, suggesting that the core is forming high-mass stars in clusters.

3.4. Multi-scale Velocity Gradients

The cloud and clump-scale velocity fields are probed using the $H^{13}CO^+$ (1–0) line emission data from the MALT90 and ATOMS surveys, respectively. The filament dynamics is retrieved by fitting single Gaussian profiles to the observed spectra retrieved over circular apertures. For the MALT90 data, these apertures are over half a beam, and for the ATOMS data, they are over one beam.

Investigating the cloud-scale velocity structure, Figure 4(a) presents the distribution of the derived velocity parameters from the MALT90 data overlaid on Spitzer 8 μm emission, where the color and size of the circle encode the velocity, and its dispersion, respectively. Longitudinal velocity gradients are clearly evident along the three hub-composing filaments and the velocity dispersion is seen to increase toward the center. The red- and blueshifted velocities, with respect to the systemic velocity of the HFS cloud, indicate filament-rooted gas motions toward us for F1 and F3 and away from us for F2. This is further emphasized in Figure 5(a). A monotonic trend is seen for the filaments within measured velocity uncertainties. The trend is decreasing toward the center for F2 but increasing for both F1 and F3. Note that the coherent trend seen in F1 suggests that the subfilaments (if any) in F1 have the nearly same velocity gradient, and thus can be treated as a single

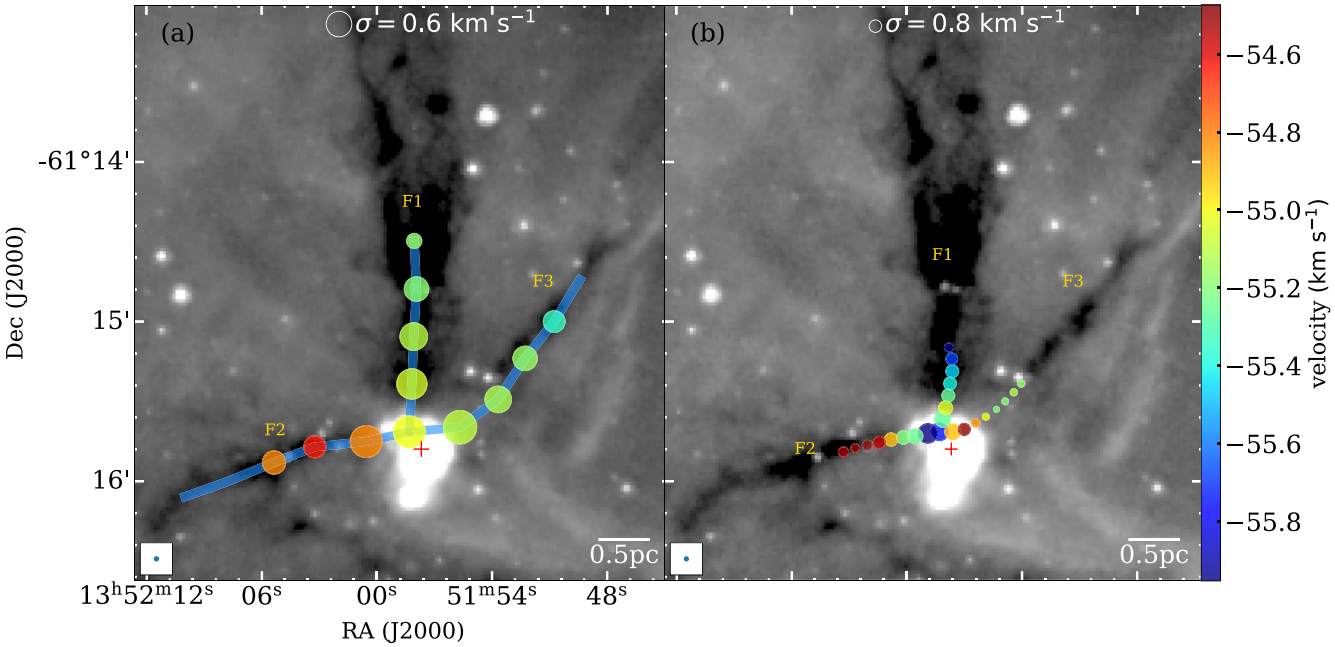

Figure 4. Distribution of the velocity and its dispersion along filaments derived from $H^{13}CO^+$ (1–0) of the MALT90 data (panel (a)) and from the same line of the ATOMS data (panel (b)). In both panels, the grayscale is the *Spitzer* 8 μm map. The color and size of the filled circles represent the velocity, and its dispersion, respectively. The blue thick lines show the filaments of the G310 HFS cloud (in panel (a)). The white empty circle in the upper middle of each panel indicates the median velocity dispersion of all measurements (circles), i.e., 0.6 km s^{-1} in panel (a) and 0.8 km s^{-1} in panel (b). The beam size of the 8 μm map and the 0.5 pc scale bar are shown at the bottom left and right corners, respectively.

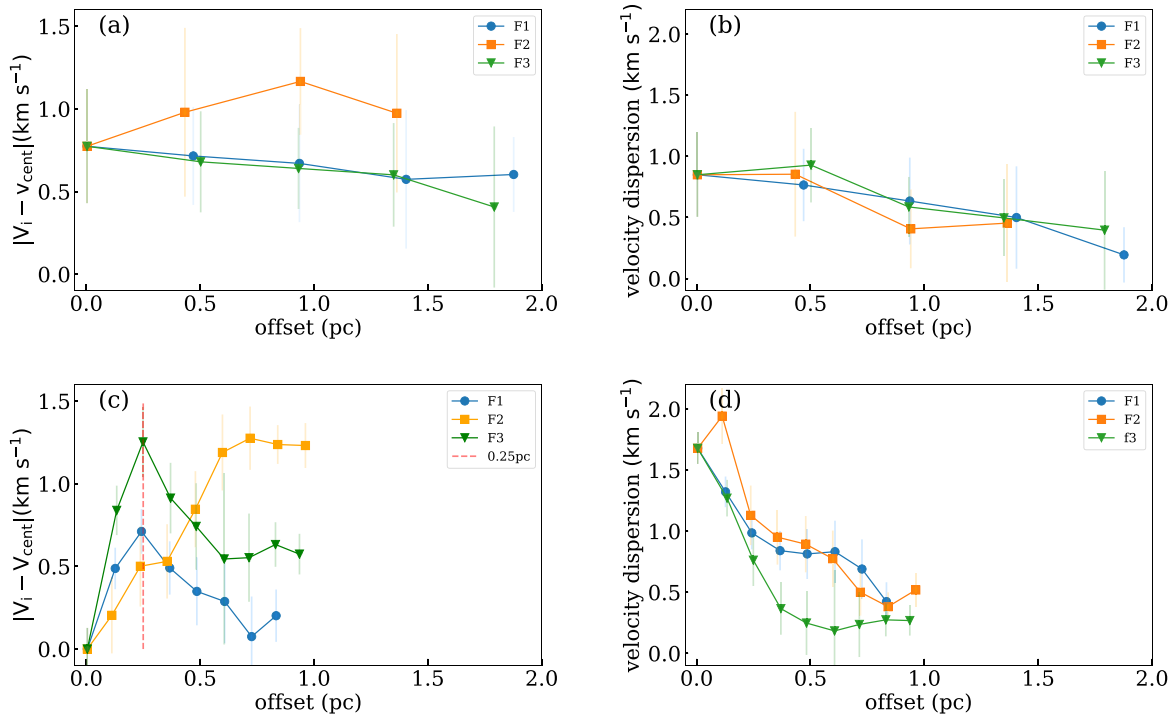

Figure 5. (a) Relative velocity of $H^{13}CO^+$ (1–0) from the MALT90 data for three filaments as a function of offset from the gravitational potential well center (the central massive core). (b) Same as panel (a) but for the velocity dispersion. (c) Same as panel (a) but for the $H^{13}CO^+$ (1–0) line from the ATOMS data. The vertical dashed line indicates the offset at which the velocity gradient trends break. (d) Same as panel (c) but for the velocity dispersion. Note that in panels (a) and (c), the same $V_{center} = -55.2$ km s^{-1} is used for comparison.

entity for kinematic analysis. The velocity gradients along the three filaments are measured from Figure 5(a) to be 0.1 ± 0.1 km s^{-1} pc^{-1} for F1, $\sim 0.2 \pm 0.1$ km s^{-1} pc^{-1} for F2, and $\sim 0.2 \pm 0.1$ km s^{-1} pc^{-1} for F3, which are presented in Table 2.

The clump-scale velocity gradient is discerned from the ATOMS data and shown in Figure 4(b). The direction of gas motion in the filaments and the velocity dispersion trend seen at the cloud scale are retained at the scale of the clump suggesting the same origin for both. However, the gradients are seen to be

Table 2
Physical Properties of Hub-composing Filaments in G310

Name	Area (pc^2)	Length (pc)	Width (pc)	M_{fil}^{a} ($M_\odot$)	M_{line} ($M_\odot$ pc^{-1})	∇_{fil}^{b} (km s^{-1} pc^{-1})	$\dot{M}_{||}$ ($10^{-4} \times M_\odot$ yr^{-1})
Filament1	7.3	5.8	1.3	3566 ± 713	620 ± 124	0.10 ± 0.02	3.6 ± 1.5
Filament2	2.4	3.3	0.7	1353 ± 271	409 ± 82	0.17 ± 0.14	2.4 ± 2.4
Filament3	3.5	4.6	0.8	777 ± 155	167 ± 34	0.18 ± 0.04	1.4 ± 0.6

Notes. Column 1: name; Column 2: area; Column 3: length; Column 4: width; Column 5: mass; Column 6: mass-per-unit-length of filament; Column 7: filament-aligned velocity gradient, which is measured from the MALT90 data (see Figure 5(a)); Column 8: mass inflow rate.

steeper than at the cloud scale. For filaments F1 and F3, a reversal is seen around 0.25 pc with a sharp increase in the velocity dispersion as well. This is likely the result of strong stellar feedback as the gas kinematics and dynamics of the inner region of the clump will be strongly influenced by the central, luminous IRAS source. The amplitudes of the velocity gradients below and above 0.25 pc in sequence are estimated to be 3.0 ± 0.6 and 0.9 ± 0.2 km s^{-1} pc^{-1} for F1, 2.2 ± 0.1 and 1.2 ± 0.3 km s^{-1} pc^{-1} for F2, and 5.2 ± 0.8 and 0.9 ± 0.3 km s^{-1} pc^{-1} for F3. It is worth noting that the dynamical parameters derived from the MALT90 and ATOMS data are different (Figure 5), where the velocities derived from the former are around 3–4 km s^{-1} blueshifted than those from the latter while the maximum velocity dispersion derived from the former is around 2 times higher than those from the latter. This could be attributed to the different beam sizes of the two data sets, where the relatively poor beam (38″) of the MALT90 data samples colder quiescent envelope gas (mostly likely blue-shifted) compared to that probed with the finer beam (∼2″) of the ATOMS data. These differences result in much shallower velocity trends on the cloud scale than on the clump scale (i.e., Figure 5(a) versus Figure 5(c)), but do not affect the general velocity trends as analyzed above.

3.5. Multi-scale Gas Infall/Accretion

The observed cloud-scale velocity gradients in G310 can be considered imprints of the filament-rooted inertial inflow onto the gravitational potential well of the HFS cloud (see below). Following Kirk et al. (2013), the parallel mass inflow rate ($\dot{M}_{fil}$) can be estimated by assuming a cylindrical filament of mass M_{fil}, and length L_{fil} at an inclination angle of ϕ with respect to the plane of the sky (45° used here). The total $\dot{M}_{fil}$ of the hub-composing filaments is estimated to be $0.7 \pm 0.5 \times 10^{-3}$ $M_\odot$ yr^{-1} (see Table 2, and Appendix B for a detailed calculation for each individual filament). This value should be a lower limit, and thus can be above $\sim 10^{-3}$ $M_\odot$ yr^{-1} if the remaining gas inflowing off the filaments within the cloud is considered (Peretto et al. 2013).

The classical infall signature of a blue asymmetric profile of the optically thick HCO^+ (1–0) transition (Liu et al. 2016) is observed for the G310 clump from the MALT90 data and displayed in Figure 6. This infall signature allows us to attribute the same trend of the cloud and clump-scale velocity gradients to the same mass infall/inflow origin. The infall velocity is estimated using the radiative transfer model "Hill5" (e.g., De Vries & Myers 2005). The fitted model is shown in Figure 6(a). The estimated value of 1.1 ± 0.6 km s^{-1} is in good agreement with those reported for clumps (e.g., Traficante et al. 2018). Subsequently, the clump-scale mass infall/accretion rate (e.g., Sanhueza et al. 2010), $\dot{M} = M_{clp} V_{clp}^{in} / R_{clp}$ is estimated to be $(2.4 \pm 1.7) \times 10^{-3}$ $M_\odot$ yr^{-1}, where M_{clp} is the enclosed mass within $R_{clp} = 0.6$ pc and V_{clp}^{in} is the infall velocity at the radius R_{clp} (see Table 1). At the core level, the ATOMS HCO^+ (1–0) transition shows a similar infall signature (see Figure 6(b)). This finds support in the detected outflows associated with the central massive core, which is evidence of core-scale gas infall onto the embedded protostar (s). Using the same approach discussed above, the infall velocity, V_{core}^{in}, and the core mass accretion rate is estimated to be (2.1 ± 0.1) km s^{-1} and $(6.5 \pm 1.3) \times 10^{-3}$ $M_\odot$ yr^{-1}, respectively, the latter being typical of high-mass star-forming cores (López-Sepulcre et al. 2010; Saha et al. 2022). The above-derived parameters for both the central clump and core are given in Columns 8 and 9 of Table 1.

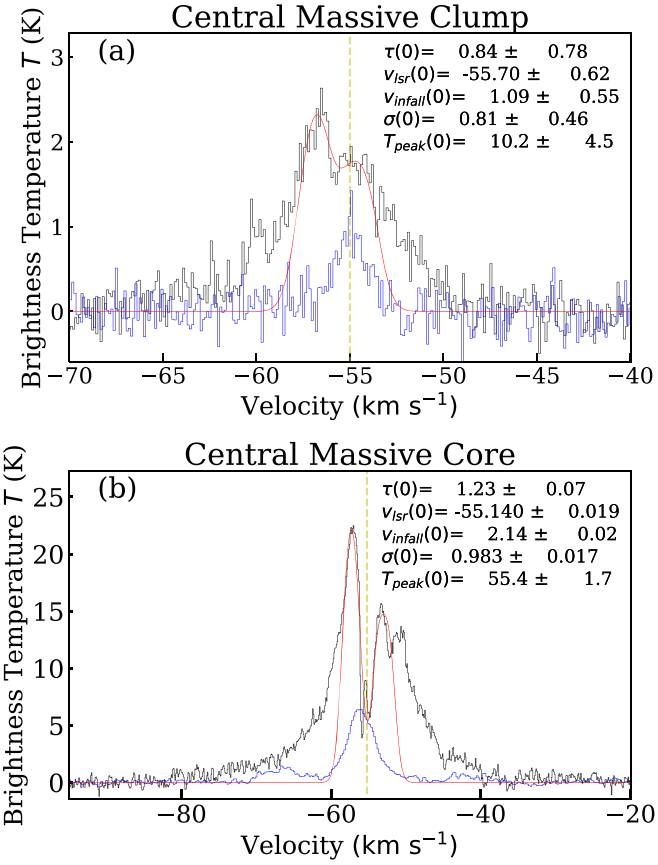

Figure 6. Average spectra of $J = 1$–0 of HCO^+ (in black) and $H^{13}CO^+$ (in blue) for the massive clump (panel (a)), and central massive core (panel (b)). The red curve represents the Hill5 model fitting while the yellow vertical line indicates the systematic velocity derived from the optically thin $H^{13}CO^+$ line. The spectra for the clump and core are extracted from the MALT90, and ATOMS data, respectively. The model-fitted parameters are given at the upper right corner of each panel.

The clump- and core-scale infall are consistent with their subvirial state. The virial parameter, $\alpha_{\rm vir} = \frac{5\sigma^2_{\rm turb}R}{GM}$ (Krumholz et al. 2005; Liu et al. 2019) where G is a gravitational constant. The turbulent velocity $\sigma_{\rm turb} \sim (0.9 \pm 0.4)$ km s^{-1} is derived from the clump-averaged $H^{13}CO^+$ (1–0) spectrum of the MALT90 survey. For the turbulent central massive core, $\sigma_{\rm turb} \sim (2.0 \pm 0.1)$ km s^{-1} derived from $H^{13}CO^+$ (1–0) of the ATOMS data. Using these values along with the estimated radius and mass (see Section 3.1), the virial parameter, $\alpha_{\rm vir}$, is calculated to be $\sim 0.4 \pm 0.1$ and $\sim 1.5 \pm 0.6$ for the clump and the core (listed in Column 7 of Table 1), respectively, satisfying at both scales $\alpha^{\rm crit}_{\rm vir} \leqslant 2$ for gravitational collapse (e.g., Kauffmann et al. 2013).

4. Discussion

4.1. Multi-scale Scenario of High-mass Star Formation

Many observational and numerical studies are gradually converging to a multi-scale mass accretion scenario for the formation of high-mass stars, and these highlight the role of HFSs in high-mass star formation (Beuther et al. 2018; Vázquez-Semadeni et al. 2019; Kumar et al. 2020; Padoan et al. 2020; Liu et al. 2022b, 2023; Saha et al. 2022). HFSs have been the focus of several statistical studies (Kumar et al. 2020; Zhou et al. 2022; Liu et al. 2023). In particular, Liu et al. (2023) studied a sample of 17 HFSs composed of two distinct evolutionary stages using high-angular resolution ($\sim 1''$–$2''$) Atacama Large Millimeter/submillimeter Array (ALMA) 1.3 mm (Li et al. 2023; Morii et al. 2023) and 3 mm continuum data (Liu et al. 2020b; Sanhueza et al. 2019). Liu et al. (2023) discuss the observed trend on multi-scales (i.e., clumps and cores) of increasing mass and mass surface density with the evolution from IR-dark to IR-bright stage, the mass-segregated cluster of young stellar objects, and the potentially preferential escape directions of outflow feedback. These observed facts strongly advocate for multi-scale mass accretion/transfer as the major agent for high-mass star formation in the HFSs.

For the G310 HFS, the smooth large-scale (cloud-scale), filament-aligned coherent velocity gradients could be due to the effect of either gravity-driven gas motion toward the central massive core, as described in the GHC model, or turbulence-driven large-scale inertial inflow discussed in the I2 model. Both models claim to facilitate mass accumulation in the hub and thus high-mass star formation therein. In the central hub region of the G310 cloud covered by the ATOMS data, the gas infall is evident through the filament-rooted velocity gradients present all the way down to the HFS center where high-mass stars form. At the core scale, the ongoing gravitational collapse results in mass accretion onto the centrally embedded luminous protostars.

The observed morphology of the G310 HFS suggests the hierarchical density structures (i.e., clouds, clumps, and cores) to be spatially connected and dynamically linked through a multi-scale, dynamical process of mass accretion. Observed in other high-mass star-forming HFS clouds (Liu et al. 2012, 2022a, 2022b; Peretto et al. 2013, 2014; Kumar et al. 2020; Avison et al. 2021; Sanhueza et al. 2021), this dynamical mass accretion process has been highlighted in the theoretical models such as GHC and I2. Of particular mention are the two most-studied high-mass HFS clouds, SDC335 (Avison et al. 2021; Olguin et al. 2021, 2022; Xu et al. 2023) and G34 (Liu et al. 2022a), which give detailed observational evidence in strong support of the theoretical predictions.

For the SDC335 HFS, the mass infall rate is similar (i.e., about $10^{-3}\ M_\odot\ {\rm yr}^{-1}$) at cloud, clump, and core scales (Avison et al. 2021; Xu et al. 2023). For the G34 HFS, the mass infall rate is around 4 times higher at the clump scale than at the core scale. However, the core-scale mass infall rate was indirectly derived from the outflow rate, without accounting for the ionized gas contribution and the exact outflow inclination angle. Hence, it is possible that the core-scale mass infall rate could be underestimated. These studies of SDC335 and G34 suggest that there is a nearly continuous, multi-scale gas inflow in the early stage of high-mass star formation in HFS clouds. From the analysis presented earlier, a similar picture can be conjectured for the G310 HFS cloud.

4.2. Comparison with Theoretical Models

Both the GHC and I2 models propose that high-mass stars form through multi-scale, dynamical mass transfer. However, the models differ in how they explain the origin of intermediate-size structures like hub-filament systems. In I2, these structures result from supersonic turbulent flows that are not driven by self-gravity (i.e., *inertial*). In the GHC, they originate from large-scale gravitational contraction of the cloud. This implies that I2 requires filaments to be formed by shocks, while GHC predicts a smooth formation process (similar to Bondi flow). In GHC, strong shocks should only occur at the hubs, where the filaments collide. In contrast, I2 predicts that shock tracers should emit along the entire length of the filaments. From Figure 3, there is no SiO detection, which traces shocks, along the whole length of the filaments. However, we cannot rule out that the expected SiO emission is below the low sensitivity (i.e., 0.2 K) of our observations. Therefore, the lack of filament-aligned SiO emission does not allow us to favor GHC over I2.

Another key difference between GHC and I2 is that GHC predicts that unbound low-mass or low-column density structures are being compressed by the infall from larger-scale bound structures (Gómez et al. 2021; Camacho et al. 2023). This implies that the virial parameter should decrease with increasing scale in hierarchically embedded structures. In Section 3.5, we show that the virial parameter in the G310 HFS decreases by more than a factor of 3 from the core to the clump scale. However, this could be due to either the compression of the filaments that form the hub, as GHC suggests, or the strong stellar feedback within the central hub's high-mass star-forming core. To rule out the latter possibility, we need to focus on HFS clouds that are quiet in star formation (e.g., IR-quiet) and perform the same multi-scale analysis of the virial parameter. It is, therefore, difficult to favor one model over the other based on the results of this study.

5. Summary and Conclusions

We present a comprehensive analysis of the hierarchical kinematics and dynamical gas motions associated with a typical HFS cloud, G310, using primarily the 3 mm continuum observation and molecular line transitions from the ATOMS survey. The cloud- and clump-scale analysis is done with MALT90 data.

Three hub-composing filaments (F1–F3, $5.7 \pm 1.1 \times 10^3\ M_\odot$ in total) are detected converging toward the central hub region. The central hub contains a massive clump ($1280 \pm 160\ M_\odot$), which harbors a massive HMC, central massive core, of mass $106 \pm 21\ M_\odot$. Five outflow lobes are identified from the

CS (2–1) and SiO (2–1) lines in the ATOMS data associated with the central massive core, suggesting high-mass star formation in a clustered environment. Multi-scale velocity gradients have been revealed from the analysis of $H^{13}CO^+$ (1–0) of both the MALT90 and ATOMS data. Coherent longitudinal velocity gradients along the filaments coupled with the signature of gravitational collapse in the central massive core, suggest continuous, multi-scale gas inflow feeding the high-mass star-forming seed(s) in the central massive core. The presence of the luminous ($L_{bol} \sim 10^{4.8}\ L_{\odot}$) IRAS source suggests strong stellar feedback, which is supported by the observed reversal of the velocity gradient in the inner (0.25 pc) region of the clump and the associated enhanced velocity dispersion. However, this does not inhibit mass accretion onto the forming central, embedded protostar(s) as evidenced by the subvirial state and infall signature of the central massive core, and its associated outflows.

Our study of a robust HFS cloud shows the importance of dynamical, multi-scale mass accretion for the high-mass protostars in the hub of HFS clouds. This supports the multi-scale scenario of high-mass star formation in both gravity-driven (GHC) and turbulence-driven (I2) models. Multi-scale gas dynamics need to be probed with higher sensitivity observations in a larger sample of HFSs, especially the ones without significant stellar feedback (e.g., IR-dark) to investigate the predictions of these models in detail.

Acknowledgments

This work has been supported by the National Key R&D Program of China (No. 2022YFA1603101). H.-L.L. is supported by the National Natural Science Foundation of China (NSFC) through grant No. 12103045, and by Yunnan Fundamental Research Project (grant No. 202301AT070118). P.S. was partially supported by a Grant-in-Aid for Scientific Research (KAKENHI Nos. JP22H01271 and JP23H01221) of JSPS. S.-L.Q. is supported by the NSFC under No. 12033005. T.L. acknowledges the support of the NSFC through grants Nos. 12073061 and 12122307. K.W. acknowledges support from the National Science Foundation of China (11973013), the China Manned Space Project (CMS-CSST-2021-A09, CMS-CSST-2021-B06), the National Key Research and Development Program of China (2022YFA1603102), and the High-performance Computing Platform of Peking University. This research was carried out in part at the Jet Propulsion Laboratory, which is operated by the California Institute of Technology under a contract with the National Aeronautics and Space Administration (80NM0018D0004). G.C.G. acknowledges the support of UNAM-PAPIIT IN103822 grant. A.P. and E.V.-S. acknowledge financial support from the UNAM-PAPIIT IG100223 grant. A.P. further acknowledges further support from the Sistema Nacional de Investigadores of CONACyT, and from CONACyT grant No. 86372 of the "Ciencia de Frontera 2019" program, entitled "Citlalcóatl: A multi-scale study at the new frontier of the formation and early evolution of stars and planetary systems," México. M.J. acknowledges support from the Academy of Finland grant No. 348342. This work is supported by the international partnership program of Chinese Academy of Sciences through grant No. 114231KYSB20200009, and Shanghai Pujiang Program 20PJ1415500. G.G., A.S., and L.B. gratefully acknowledge the support of the ANID BASAL projects ACE210002 and FB210003. A.S. further gratefully acknowledges support by the Fondecyt Regular (projectcode 1220610). K.T. was supported by JSPS KAKENHI (Grant Number JP20H05645). C.W.L. is supported by the Basic Science Research Program through the National Research Foundation of Korea (NRF) funded by the Ministry of Education, Science and Technology (NRF-2019R1A2C1010851), and by the Korea Astronomy and Space Science Institute grant funded by the Korea government (MSIT; Project No. 2023-1-84000). This paper makes use of the following ALMA data: ADS/JAO.ALMA#2019.1.00685.S and 2015.1.01539.S. ALMA is a partnership of ESO (representing its member states), NSF (USA), and NINS (Japan), together with NRC (Canada), MOST and ASIAA (Taiwan), and KASI (Republic of Korea), in cooperation with the Republic of Chile. The Joint ALMA Observatory is operated by ESO, AUI/NRAO, and NAOJ. This research made use of astrodendro, a Python package to compute dendrograms of Astronomical data (http://www.dendrograms.org/). This research made use of Astropy, a community-developed core Python package for Astronomy (Price-Whelan et al. 2018).

Appendix A
Generating De-noised Data Cube of $H^{13}CO^+$ (1–0) and Moment Maps

To reduce the effect of the noise of the observed data on gas emission analysis, we produced a de-noised/modeled $H^{13}CO^+$ data cube using the BTS algorithm (Clarke et al. 2018). It is an automated routine that can model multiple (up to six) velocity components in spectral lines. Here, the number of the components and their positions (in the velocity/frequency axis) is determined by deriving the first, second, and third derivatives of a spectrum. The routine then adopts a least-squares fitting approach to refine the fit with the determined component number, checking for overfitting and overlapping velocity centroids. As default inputs to BTS, we used $\alpha_{BTS} = 3$ (the channel number over which the spectrum is smoothed, see Clarke et al. 2018), $\beta_{BTS} = 5$ (signal-to-noise threshold for a velocity component) and $\gamma_{BTS} = 1.5$ (fitting acceptance threshold). As outputs, the BTS algorithm yields the amplitude (I_c, in units of jansky per beam per kilometers per second), velocity centroid (V_c in units of kilometers per second), and dispersion (σ_c in units of kilometers per second) of each component, c. Based on the average spectrum of $H^{13}CO^+$ (1–0) over the central hub region, the velocity range of the modeled spectra was set to be $[-57.5, -52.5]\ km\ s^{-1}$. In this range, the fraction of the one and two velocity components in the total fitted spectra is 96%, and 5%, respectively. This result indicates that $H^{13}CO^+$ (1–0) line emission of the central hub region is characterized mostly as a single velocity component, which interprets well the observed single-peaked average spectrum over the same region (see above).

Following Pan et al. (2023), the moment maps (moments 0, 1, and 2) were created from the modeled/de-noised $H^{13}CO^+$ (1–0) cube that was constructed from the BTS-modeled parameters (I_c, V_c, and σ_c). The velocity-integrated intensity, moment 0, satisfies $m0 = \int I dV$ where the integration is conducted over $[-57.5, -52.5]\ km\ s^{-1}$. Moment 1, the intensity-weighted mean velocity, was given by the form $\sum_{i=1}^{N} m0_{c,i}\ V_{c,\ i} / \sum_{i=1}^{N} m0_{c,i}$ for N components ($m0_{c,i}$ and $V_{c,\ i}$ referred as to the integrated intensity, and velocity centroid of the ith component, respectively). With a similar weighting approach, moment 2, defined as the velocity dispersion, was

calculated as $\sum_{i=1}^{N} m0_{c,i}\ \sigma_{c,\ i} / \sum_{i=1}^{N} m0_{c,i}$ for N components ($\sigma_{c,\ i}$ corresponding to the velocity dispersion of the ith component).

Appendix B
Cloud-scale Gas Infalling/Accretion Rates

Following Kirk et al. (2013), the filament-rooted (parallel) mass inflow rate can be estimated by assuming a cylinder of filament mass $M_{\rm fil}$, and length $L_{\rm fil}$ at an inclination angle of ϕ to the plane of the sky (PoS; 0° for being parallel to the PoS and 90° for being along the line of the sight (LoS), 0° used here). The filament-aligned (parallel) mass accretion rate, $\dot{M}_{\parallel}$, is written in the form $\dot{M}_{\parallel} = \frac{M_{\rm fil} \nabla V_{\parallel,\rm fil}}{\tan(\phi)}$, where $\nabla V_{\parallel,\rm obs}$ is the filament-aligned velocity gradient, related to $V_{\parallel,\rm fil}$ via the form $V_{\parallel,\rm fil}/L_{\rm fil}$.

The filament mass for F1–F3 was derived from the 18″ H_2 column density ($N(H_2)$) map that was created from Herschel data. For the details of the map making refer to Peretto et al. (2016) and Pan et al. (2023). In a nutshell, the ratio of the Herschel 160–250 μm images was used as a dust temperature ($T_{\rm d}$) tracer and the derived temperature was then used together with the 250 μm image to calculate the column density ($N(H_2)$) map, where the dust opacity law $\kappa_\nu = 0.1 \times (\nu/1\ {\rm THz})^{\beta}$ was adopted along with $\beta = 2$, and a gas-to-dust mass ratio of 100 (Beckwith et al. 1990). The $N(H_2)$ map enables the full spatial coverage of the G310 HFS cloud, allowing it to count the full mass of the hub-composing filaments. The boundary of each filament is depicted roughly based on a column density level of $1.5 \times 10^{22}\ {\rm cm}^{-2}$, as indicated in the gray polygon in Figure 1. In practice, a constant level of $1.0 \times 10^{22}\ {\rm cm}^{-2}$ as background emission was subtracted from the $N(H_2)$ map for the mass estimate. Accordingly, the enclosed mass of each filament was estimated to be $3.6 \pm 0.7 \times 10^3\ M_\odot$ for F1, $1.4 \pm 0.3 \times 10^3\ M_\odot$ for F2, and $0.8 \pm 0.2 \times 10^3\ M_\odot$ for F3. Given the $\nabla V_{\parallel,\rm obs}$ values (see Section 3.4 and Figure 5(a)), we obtain longitudinal mass inflow rates (see Table 2) of $(3.6 \pm 1.5) \times 10^{-4}\ M_\odot\ {\rm yr}^{-1}$ for F1, $(2.4 \pm 2.4) \times 10^{-4}\ M_\odot\ {\rm yr}^{-1}$ for F2, and $(1.4 \pm 0.6) \times 10^{-4}\ M_\odot\ {\rm yr}^{-1}$ for F3.

ORCID iDs

Hong-Li Liu https://orcid.org/0000-0003-3343-9645
Anandmayee Tej https://orcid.org/0000-0001-5917-5751
Tie Liu https://orcid.org/0000-0002-5286-2564
Patricio Sanhueza https://orcid.org/0000-0002-7125-7685
Sheng-Li Qin https://orcid.org/0000-0003-2302-0613
Xing Lu https://orcid.org/0000-0003-2619-9305
Ke Wang https://orcid.org/0000-0002-7237-3856
Feng-Wei Xu https://orcid.org/0000-0001-5950-1932
Enrique Vázquez-Semadeni https://orcid.org/0000-0002-1424-3543
Shanghuo Li https://orcid.org/0000-0003-1275-5251
Gilberto C. Gómez https://orcid.org/0000-0003-4714-0636
Aina Palau https://orcid.org/0000-0002-9569-9234
Paul F. Goldsmith https://orcid.org/0000-0002-6622-8396
Mika Juvela https://orcid.org/0000-0002-5809-4834
Anindya Saha https://orcid.org/0000-0002-9793-3039
Leonardo Bronfman https://orcid.org/0002-9574-8454
Chang Won Lee https://orcid.org/0000-0002-3179-6334
Ken'ichi Tatematsu https://orcid.org/0000-0002-8149-8546
Lokesh Dewangan https://orcid.org/0000-0001-6725-0483
Yong Zhang https://orcid.org/0000-0002-1086-7922
Amelia Stutz https://orcid.org/0000-0003-2300-8200
L. Viktor Toth https://orcid.org/0000-0002-5310-4212
James O. Chibueze https://orcid.org/0000-0002-9875-7436

References

André, P., Men'shchikov, A., Bontemps, S., et al. 2010, A&A, 518, L102
Avison, A., Fuller, G. A., Peretto, N., et al. 2021, A&A, 645, A142
Beckwith, S. V. W., Sargent, A. I., Chini, R. S., & Guesten, R. 1990, AJ, 99, 924
Benjamin, R. A., Churchwell, E., Babler, B. L., et al. 2003, PASP, 115, 953
Beuther, H., Mottram, J. C., Ahmadi, A., et al. 2018, A&A, 617, A100
Brand, J., & Blitz, L. 1993, A&A, 275, 67
Bronfman, L., Nyman, L. A., & May, J. 1996, A&AS, 115, 81
Camacho, V., Vázquez-Semadeni, E., Zamora-Avilés, M., & Palau, A. 2023, MNRAS, 523, 3376
Clarke, S. D., Whitworth, A. P., Spowage, R. L., et al. 2018, MNRAS, 479, 1722
Cyganowski, C. J., Whitney, B. A., Holden, E., et al. 2008, AJ, 136, 2391
De Buizer, J. M., Liu, M., Tan, J. C., et al. 2017, ApJ, 843, 33
De Vries, C. H., & Myers, P. C. 2005, ApJ, 620, 800
Faúndez, S., Bronfman, L., Garay, G., et al. 2004, A&A, 426, 97
Foster, J. B., Jackson, J. M., Barnes, P. J., et al. 2011, ApJS, 197, 25
Foster, J. B., Rathborne, J. M., Sanhueza, P., et al. 2013, PASA, 30, e038
Gómez, G. C., Vázquez-Semadeni, E., & Palau, A. 2021, MNRAS, 502, 4963
Green, J. A., Caswell, J. L., Fuller, G. A., et al. 2012, MNRAS, 420, 3108
Jackson, J. M., Rathborne, J. M., Foster, J. B., et al. 2013, PASA, 30, e057
Kauffmann, J., Pillai, T., & Zhang, Q. 2013, AAS Meeting, 221, 332.03
Kirk, H., Myers, P. C., Bourke, T. L., et al. 2013, ApJ, 766, 115
Krumholz, M. R., McKee, C. F., & Klein, R. I. 2005, Natur, 438, 332
Kumar, M. S. N., Palmeirim, P., Arzoumanian, D., & Inutsuka, S. I. 2020, A&A, 642, A87
Li, S., Sanhueza, P., Zhang, Q., et al. 2023, ApJ, 949, 109
Liu, H. B., Jiménez-Serra, I., Ho, P. T. P., et al. 2012, ApJ, 756, 10
Liu, T., Kim, K.-T., Yoo, H., et al. 2016, ApJ, 829, 59
Liu, H.-L., Stutz, A., & Yuan, J.-H. 2019, MNRAS, 487, 1259
Liu, H.-L., Sanhueza, P., Liu, T., et al. 2020a, ApJ, 901, 31
Liu, T., Evans, N. J., Kim, K.-T., et al. 2020b, MNRAS, 496, 2790
Liu, H.-L., Liu, T., Evans, N. J. I., et al. 2021, MNRAS, 505, 2801
Liu, H.-L., Tej, A., Liu, T., et al. 2022b, MNRAS, 511, 4480
Liu, H.-L., Tej, A., Liu, T., et al. 2022a, MNRAS, 510, 5009
Liu, H.-L., Tej, A., Liu, T., et al. 2023, MNRAS, 522, 3719
López-Sepulcre, A., Cesaroni, R., & Walmsley, C. M. 2010, A&A, 517, A66
Molinari, S., Swinyard, B., Bally, J., et al. 2010, A&A, 518, L100
Morii, K., Sanhueza, P., Nakamura, F., et al. 2023, ApJ, 950, 148
Myers, P. C. 2009, ApJ, 700, 1609
Olguin, F. A., Sanhueza, P., Guzmán, A. E., et al. 2021, ApJ, 909, 199
Olguin, F. A., Sanhueza, P., Ginsburg, A., et al. 2022, ApJ, 929, 68
Ossenkopf, V., & Henning, T. 1994, A&A, 291, 943
Padoan, P., Pan, L., Juvela, M., Haugbølle, T., & Nordlund, A. 2020, ApJ, 900, 82
Pan, S., Liu, H.-L., & Qin, S.-L. 2023, MNRAS, 519, 3851
Peretto, N., Fuller, G. A., Duarte-Cabral, A., et al. 2013, A&A, 555, A112
Peretto, N., Fuller, G. A., André, P., et al. 2014, A&A, 561, A83
Peretto, N., Lenfestey, C., Fuller, G. A., et al. 2016, A&A, 590, A72
Price-Whelan, A. M., Sipőcz, B. M., Astropy Collaboration, et al. 2018, AJ, 156, 123
Purser, S. J. D., Lumsden, S. L., Hoare, M. G., & Cunningham, N. 2018, MNRAS, 475, 2
Reid, M. J., Menten, K. M., Brunthaler, A., et al. 2019, ApJ, 885, 131
Reid, M. J., Menten, K. M., Brunthaler, A., et al. 2014, ApJ, 783, 130
Saha, A., Tej, A., Liu, H.-L., et al. 2022, MNRAS, 516, 1983
Sanhueza, P., Contreras, Y., Wu, B., et al. 2019, ApJ, 886, 102
Sanhueza, P., Garay, G., Bronfman, L., et al. 2010, ApJ, 715, 18
Sanhueza, P., Girart, J. M., Padovani, M., et al. 2021, ApJL, 915, L10
Sanhueza, P., Jackson, J. M., Zhang, Q., et al. 2017, ApJ, 841, 97
Schuller, F., Menten, K. M., Contreras, Y., et al. 2009, A&A, 504, 415
Traficante, A., Duarte-Cabral, A., Elia, D., et al. 2018, MNRAS, 477, 2220
Urquhart, J. S., Hoare, M. G., Lumsden, S. L., et al. 2009, A&A, 507, 795
Urquhart, J. S., Figura, C. C., Moore, T. J. T., et al. 2014, MNRAS, 437, 1791
Vázquez-Semadeni, E., Palau, A., Ballesteros-Paredes, J., Gómez, G. C., & Zamora-Avilés, M. 2019, MNRAS, 490, 3061
Walsh, A. J., Burton, M. G., Hyland, A. R., & Robinson, G. 1998, MNRAS, 301, 640
Wenger, T. V., Balser, D. S., Anderson, L. D., & Bania, T. M. 2018, ApJ, 856, 52
Xu, F.-W., Wang, K., Liu, T., et al. 2023, MNRAS, 520, 3259
Zhou, J.-W., Liu, T., Evans, N. J., et al. 2022, MNRAS, 514, 6038